

# Materials Advances

Accepted Manuscript

This article can be cited before page numbers have been issued, to do this please use: R. J. Awan, Z. Ertekin, S. Çitolu, H. Duran, S. N. Arshad and M. D. Symes, *Mater. Adv.*, 2026, DOI: 10.1039/D6MA00599C.



This is an Accepted Manuscript, which has been through the Royal Society of Chemistry peer review process and has been accepted for publication.

Accepted Manuscripts are published online shortly after acceptance, before technical editing, formatting and proof reading. Using this free service, authors can make their results available to the community, in citable form, before we publish the edited article. We will replace this Accepted Manuscript with the edited and formatted Advance Article as soon as it is available.

You can find more information about Accepted Manuscripts in the [Information for Authors](#).

Please note that technical editing may introduce minor changes to the text and/or graphics, which may alter content. The journal's standard [Terms & Conditions](#) and the [Ethical guidelines](#) still apply. In no event shall the Royal Society of Chemistry be held responsible for any errors or omissions in this Accepted Manuscript or any consequences arising from the use of any information it contains.

# Hollow nickel ferrite nanofibers templated using waste expanded polystyrene as electrocatalysts of the hydrogen evolution reaction

Rabiya J. Awan,<sup>a,b</sup> Zeliha Ertekin,<sup>a</sup> Senem Çitoğlu,<sup>c</sup> Hatice Duran,<sup>c,d</sup> Salman N. Arshad<sup>\*b,e,f</sup> and Mark D. Symes<sup>\*a</sup>

<sup>a</sup>School of Chemistry, University of Glasgow, Glasgow, G12 8QQ, United Kingdom

<sup>b</sup>Department of Chemistry and Chemical Engineering, Syed Babar Ali School of Science and Engineering, Lahore University of Management Sciences, Lahore 54792, Pakistan

<sup>c</sup>Department of Materials Science & Nanotechnology Engineering, TOBB University of Economics and Technology, Söğütözü Cad. 43, Ankara, 06560 Türkiye

<sup>d</sup>UNAM — National Nanotechnology Research Center and Institute of Materials Science and Nanotechnology, Bilkent University, Ankara, 06800 Türkiye

<sup>e</sup>Department of Materials Science and Engineering, King Fahd University of Petroleum & Minerals, Dhahran, Saudi Arabia

<sup>f</sup>Center for Hydrogen Technologies and Carbon Management, King Fahd University of Petroleum & Minerals, Dhahran, Saudi Arabia

## Abstract

The electrochemical hydrogen evolution reaction is a process of central importance to a future hydrogen economy and the de-fossilization of various industrial processes. To operate with high efficiency, electrocatalysts are required for this reaction, of which Pt is the best known to date. However, due to its scarcity and the ongoing environmental cost of mining precious metals, the development of alternatives based on first row transition metals is an area of very intense interest. Whilst the performance of such earth-abundant catalysts cannot compete with Pt on an atom-for-atom basis, engineering the morphology of first row transition metal catalysts can produce significant improvements in performance relative to the bulk solids. Herein, we highlight one such example, whereby multichannel carbon nanofibers (formed using waste polystyrene as a key component) were used to template the formation of hollow NiFe<sub>2</sub>O<sub>4</sub> nanofibers with a surface area (167 m<sup>2</sup>/g), which was nearly double that of pristine NiFe<sub>2</sub>O<sub>4</sub> (81 m<sup>2</sup>/g). The material was thoroughly characterized by a range of methods and was found to exhibit significantly enhanced activity for the hydrogen evolution reaction: in linear sweep voltammetry, the porous hollow NiFe<sub>2</sub>O<sub>4</sub> nanofibers required an overpotential of 178 ± 3 mV to deliver a current density of 50 mA cm<sup>-2</sup>, compared to 342 ± 2 mV for the pristine NiFe<sub>2</sub>O<sub>4</sub>



material. The results showcase the advantages of morphological control of catalysts for improving hydrogen evolution activity.

**Keywords:** *Electrospinning; polystyrene; hollow nanofiber; nickel ferrite; hydrogen evolution reaction.*

## 1. Introduction

Hydrogen, as an environmentally friendly and renewable energy carrier, has gained considerable attention for its potential as a clean-burning fuel.<sup>1-2</sup> One of the most promising ways to produce hydrogen is through water splitting, a process that breaks water into oxygen and hydrogen using renewable energy.<sup>3-4</sup> The catalysts used to drive the half-reactions of water splitting have a significant effect on the efficiency of this process. While precious metals like platinum have traditionally been favoured for the hydrogen evolution reaction due to their excellent catalytic properties, their high cost and limited availability have led scientists to seek more sustainable and affordable alternatives.<sup>5-6</sup> At high pH, first-row transition metals such as cobalt, iron, nickel, and manganese are viable substitutes, offering a balance between performance and cost<sup>7-9</sup>. Among these, spinel ferrite nanoparticles stand out due to high catalytic efficiency<sup>10</sup>, ease of synthesis<sup>11</sup>, and long-term stability. Their electrocatalytic performance is enhanced by the synergistic effects of their electronic structure and the redox behaviour of cations such as  $\text{Fe}^{3+}/\text{Fe}^{2+}$  at octahedral and tetrahedral sites.<sup>12-13</sup> However, a common issue with transition metal catalysts, including nickel ferrite, is the tendency of metal nanoparticles to agglomerate during reactions, which reduces their effectiveness over time.<sup>14-</sup>

15

To overcome this issue, researchers have focused on developing composites that combine transition metals with carbon nanomaterials.<sup>16</sup> These composites boost catalytic performance by providing a conductive matrix that prevents nanoparticle agglomeration, improves dispersion, and helps maintain their activity over extended use.<sup>17</sup> Deng et al. synthesized a composite by encapsulating a CoNi alloy in thin N-doped graphene shells (CoNi@CN) using a bottom-up approach, achieving hydrogen evolution with an overpotential of 142 mV at 10  $\text{mA cm}^{-2}$  in acidic media.<sup>18</sup> Similarly, Yunfeng Qiu et al. fabricated hierarchical N-doped carbon nanotubes on carbon nanowires derived from polypyrrole grown on carbon cloth, to



support NiCo oxides/sulfides, demonstrating an overpotential of 110 mV for hydrogen evolution at a current density of 10 mA cm<sup>-2</sup>.<sup>19</sup>

Within carbon nanomaterials, carbon nanofibers have proven to be effective supports for catalysts.<sup>20</sup> Carbon nanofibers provide a unique structure that facilitates electron transfer, ensures structural stability, and offers a large surface area for catalytic reactions.<sup>21-23</sup> Among the different types of nanofibers, porous, tube-in-tube, and hollow architectures show superior electrocatalytic activity and efficiency by allowing better dispersion of metal nanoparticles, improved reactant access, and higher current density.<sup>24-26</sup> Gao et al. developed N and P co-doped hollow carbon nanofibers using coaxial electrospinning, producing a hierarchically-porous structure that enhances electrolyte/reactant diffusion and mass transfer during electrocatalysis, leading to improved trifunctional activity (oxygen reduction, oxygen evolution, and hydrogen evolution) compared to pristine carbon nanofibers.<sup>27</sup> In addition, hierarchical vertical nanostructures grown on such conductive substrates could be beneficial for enhanced charge and mass transport due to deep diffusion characteristics and the abundance of catalytically active sites.<sup>28-30</sup>

Traditionally, polymethylmethacrylate, polylactic acid, and polyvinylpyrrolidone have been used as sacrificial polymers for porous hollow material fabrication due to their well-defined decomposition and good solubility.<sup>31</sup> However, given that the polymers are being used in a sacrificial sense, demonstrating that similar results can be achieved using waste materials would be highly advantageous as compared to using pristine polymers, by reusing materials that would otherwise be discarded. Of the 32 million tons of Styrofoam produced annually, only about 1-2% are recycled globally.<sup>32</sup> The low density of Styrofoam makes large-scale recycling economically impractical, contributing to environmental pollution.<sup>33</sup> As a result, around 80% of it ends up in landfills, where it can take 500 years or more to naturally decompose.<sup>34</sup>

In this paper, we present our findings on the synthesis, characterization, and catalytic performance of porous hollow nickel ferrite nanofibers (where the carbon template component was derived from waste Styrofoam used in chemical packaging) for hydrogen production through electrolytic water splitting. Table 1 illustrates a comparison of the electrocatalytic activity for the hydrogen evolution reaction of the resulting porous hollow nickel ferrite nanofibers with previously reported results from the literature for Ni-Fe based electrocatalysts employing other carbon supports.



**Table 1:** Comparison of the electrocatalytic performance of the hollow porous NiFe<sub>2</sub>O<sub>4</sub> nanofibers reported herein in 1 M KOH with that of previously reported catalysts.

Entry	Material	Overpotential at 10 mA cm <sup>-2</sup> (mV)*	Tafel slope (mV dec <sup>-1</sup> )	Ref.
1	Porous hollow NiFe <sub>2</sub> O <sub>4</sub> nanofibers**	58	78	This work
2	Ni <sub>3</sub> Fe nanoparticles in N-doped carbon nanotube-grafted carbon nanofibers (Ni <sub>3</sub> Fe-CNT@CF)	72	98	35
3	Core-shell-Ni <sub>3</sub> Fe(OH) <sub>9</sub> /Ni <sub>3</sub> Fe hybrid nanostructures	217	83	36
4	Nickel-iron/nanocarbon hybrids (Ni <sub>0.9</sub> Fe <sub>0.1</sub> /NC)	219	111	37
5	N-doped graphene/NiFe <sub>2</sub> O <sub>4</sub>	184	83	38
6	NiFe-double layer hydroxide carbon nanotubes	269	67	39
7	Ni-NiFe <sub>2</sub> O <sub>4</sub> @C	217	96	40
8	3D NiFe-carbon nanofiber-carbon foam	70	139	41
9	NiFe <sub>2</sub> O <sub>4</sub> /Ti <sub>3</sub> C <sub>2</sub> (MXenes)	173	112	42
10	Fe doped Ni <sub>3</sub> Fe/NiFe <sub>2</sub> O <sub>4</sub> hetero nanoparticle decorated carbon nanotubes	128	68	43
11	NiFe-Oxide Nanocubes	197	130	44

\* All values reported by linear sweep voltammetry

\*\* For comparison, the overpotential at 10 mA cm<sup>-2</sup> (mV) by bulk electrolysis is 83

## 2. Results and Discussion

The overall synthetic procedure for producing the hierarchically hollow porous NiFe<sub>2</sub>O<sub>4</sub> nanofibers is schematically illustrated in **Figure 1** (see Supporting Information Figure S1 and Table S1 for characterisation of the polystyrene starting material). In the first step of electrospinning, polyacrylonitrile and polystyrene separate into two distinct microscale phases in the precursor solution. This separation is influenced by Hansen solubility parameters, which help determine how well one material dissolves in another and their relative energy differences in the solution (see Supplementary Information).<sup>45</sup> The relative energy difference value of polyacrylonitrile is 0.82, indicating that the polymer will dissolve easily in the dimethyl



formaldehyde, while that of polystyrene is 1.03, which illustrates that dissolution of the solute in the solvent will not be good.<sup>46</sup> Hence, they both exist as two separate phases throughout the fiber. Polystyrene thermally degrades at temperatures across the range 310 °C – 460 °C.<sup>47</sup> Thus, when the sample was thermally treated at 800 °C, the polystyrene degraded, leaving behind polyacrylonitrile-derived nitrogen-doped multichannel carbon nanofibers.

The surface of these fibers was activated using acidified  $\text{KMnO}_4$ , which oxidizes the surface generating functional groups such as carboxylic acids. These groups, in turn, provide sites for the deposition of nickel ferrite. FTIR spectroscopy was used to probe the surface functionalization of both the activated and inactivated samples as shown in **Figure S2**. In the case of activated multichannel carbon nanofibers, the spectrum is dominated by a broad feature, which is ascribed to O–H ( $3317\text{ cm}^{-1}$ ) vibrations. The presence of this group typically results in increased hydrophilicity. The FTIR also shows the emergence of a new peak at  $1597\text{ cm}^{-1}$  after activation, characteristic of C=O bonding, which is an indication of the formation of a carbonyl group on the surface.<sup>48</sup> The calcination of the sample after the deposition of nickel and iron on the surface of the multichannel carbon nanofibers then transformed the core multichannel fiber into a hollow structure by conversion of carbon to  $\text{CO}_2$  (which then leaves behind a hollow  $\text{NiFe}_2\text{O}_4$  fiber).

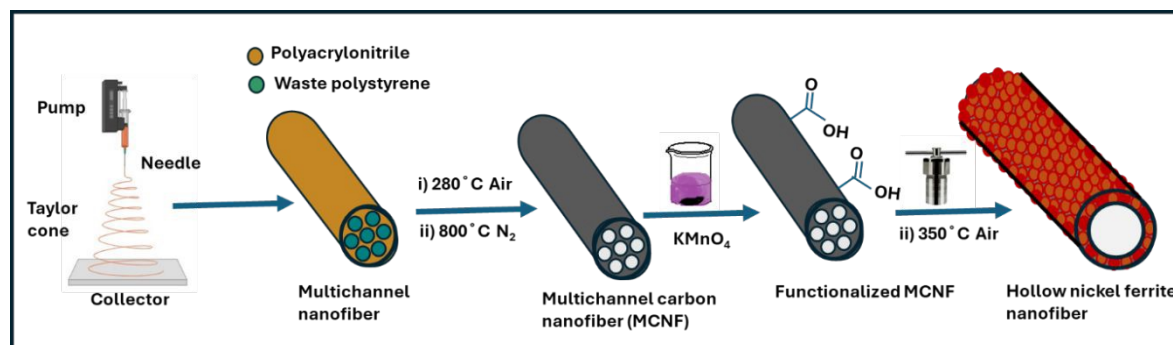


**Figure 1:** Schematic diagram for the synthesis of hollow porous nickel ferrite nanofibers.

## 2.1 Physical characterization

**Figure 2(a-d)** shows the morphology of the resulting hollow nickel ferrite nanofibers. The SEM images indicate the deposition of fine nickel ferrite platelets with an average size of  $38.2 \pm 1.6\text{ nm}$  on the surface calculated using ImageJ software. The cross-sectional SEM of the catalyst shows a clear hollow tube formed at the core of the nanofiber. The overall size of the nanofibers is  $752 \pm 78\text{ nm}$ . The energy dispersive X-ray (EDX) and elemental mapping data in



**Figure 2(e-h)** suggest that the Ni, Fe, O, and C are well mixed in the sample. Moreover, the mole percentages of Fe and Ni calculated from the EDX spectrum **Figure 2(j)** correlate well with the theoretical composition of nickel ferrite. Transmission electron microscopy (TEM) was performed to gain further insight into the nanostructure of the hollow nickel ferrite nanofibers. TEM imagery, **Figure 3(a-c)**, confirms the  $\text{NiFe}_2\text{O}_4$  nanofibers are homogeneously hollow from inside, with an inner diameter of about 470 nm. In addition,  $\text{NiFe}_2\text{O}_4$  platelets are homogeneously decorated on the inner and outer surfaces and appear transparent, further indicating their very thin nature. The  $\text{NiFe}_2\text{O}_4$  nanoplatelets on the outer surface were primarily oriented perpendicular to the surface of the nanofiber, which is beneficial for enhanced charge and mass transport due to deep diffusion characteristics.<sup>29</sup> The SEM of pristine nickel ferrite in **Figure S3(a-b)** shows agglomeration of the particles while EDX and elemental mapping in **Figure S3(c-g)** confirm its composition. The SEM **Figure S4 (a-d)** and TEM data (e-f) of the multichannel carbon nanofibers suggest the formation of surface pores (as seen by the roughness of the surface) and multiple hollow channels at the core of the fiber. The average diameter of these fibers is  $625 \pm 12$  nm, which was calculated using ImageJ software. The elemental mapping in **Figure S4(g-j)** supports the assertion of the doping of nitrogen along with carbon and oxygen.

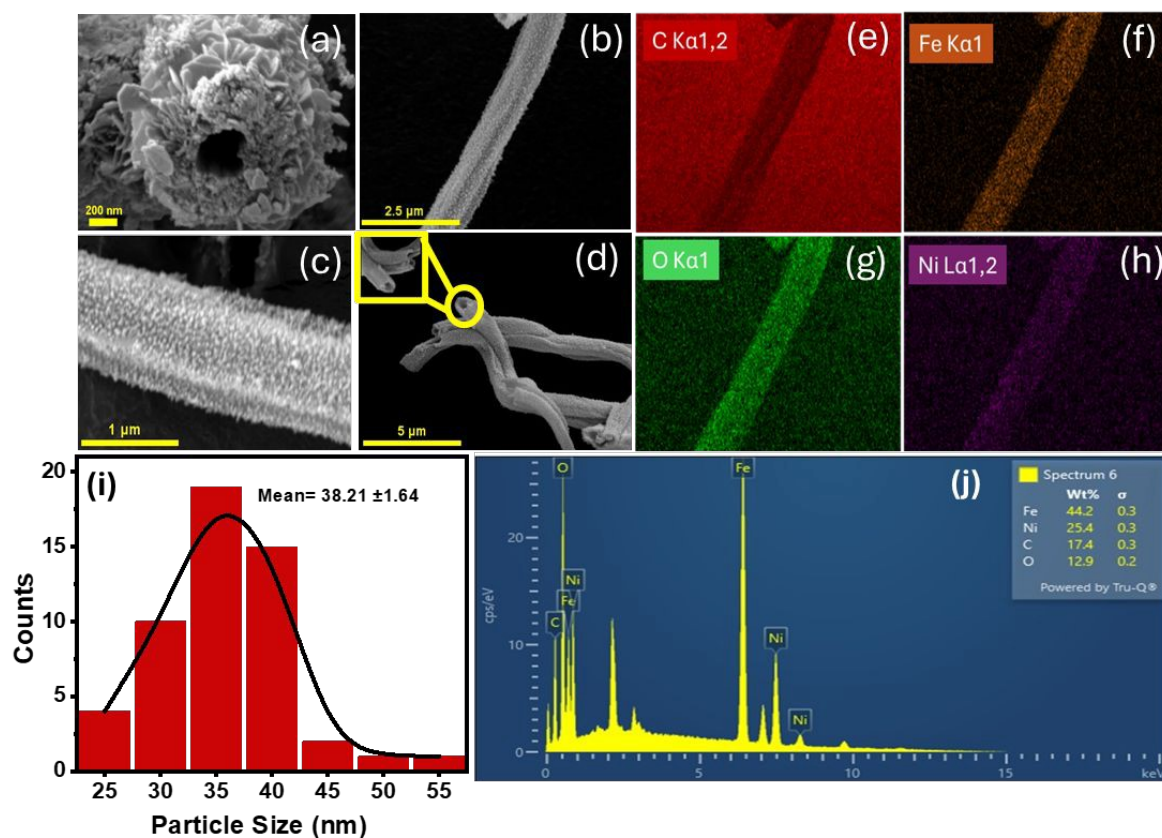


**Figure 2:** (a-d) Cross sectional SEM images of hollow NiFe<sub>2</sub>O<sub>4</sub> nanofibers at various magnifications; (e-h) elemental maps of C, Fe, O, and Ni present in the sample; (i) size distributions of the NiFe<sub>2</sub>O<sub>4</sub> nanofibers with mean and standard deviation; (j) EDX data for the hollow NiFe<sub>2</sub>O<sub>4</sub> nanofibers.

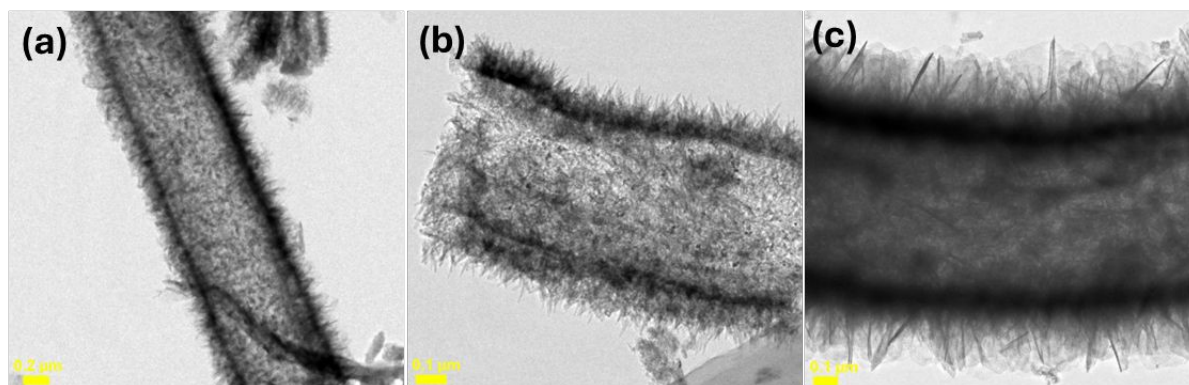


**Figure 3 (a-c)** TEM images of the porous hollow nickel ferrite nanofibers.

Figure 4 shows the XRD patterns of all the samples. The XRD pattern of the pristine multichannel carbon nanofibers shows a broad distinct diffraction peak at 25.46° which is attributed to the (002) plane of the graphitic carbon in the carbon nanofibers.<sup>49</sup> The broad peak is the characteristic feature of the amorphous material, reflecting the lack of long-range periodicity due to the presence of carbon only. Similarly, the XRD pattern of porous hollow NiFe<sub>2</sub>O<sub>4</sub> nanofiber shows peaks at 18.41°, 30.13°, 35.46°, 37.06°, 43.11°, 53.63°, 57.04°, 62.79°, 74.97°, and 79.34° corresponding to the (111), (200), (311), (222), (400), (422), (511), (440), (533), and (444) planes, respectively. The data coincides well with the cubic spinel structure of ferrites with Fd-3m space group matching with the standard JCPDS data (01-086-2267) of spinel-phase face-centered cubic (fcc) particles of NiFe<sub>2</sub>O<sub>4</sub>.<sup>50</sup> The XRD pattern of pristine nickel ferrite is also consistent with the same JCPDS reference.<sup>51</sup> The average crystallite size of the hollow porous nickel ferrite nanofibers was estimated to be 54.09 Å (~5.4 nm) using the Scherrer equation (see Supplementary Information S2), confirming the nanocrystalline nature of the material. Such small crystallite dimensions are well known to result in significant peak broadening in XRD patterns.<sup>52</sup> Therefore, the broadened diffraction peaks observed for the hollow nanofibers are attributed primarily to size-induced broadening and possible lattice strain associated with the hollow fibrous architecture. In contrast, the pristine nickel ferrite nanoparticles exhibit a larger crystallite size of 148.51 Å (~14.9 nm), resulting in comparatively sharper and more intense diffraction peaks. Despite the peak broadening in the nanofibers, all the major diffraction peaks can be well indexed to the cubic spinel structure of nickel ferrite,



with no detectable secondary phases, confirming successful phase formation in both samples. In particular, the reflections in the  $2\theta$  range of  $\sim 35\text{--}38^\circ$  appear merged in the hollow nanofiber sample, whereas they are clearly resolved in the pristine one, further supporting the effect of reduced crystallite size rather than diminished crystallinity.

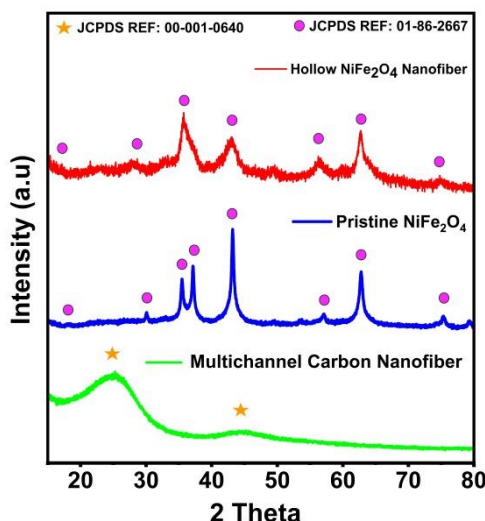


**Figure 4:** XRD patterns of all materials along with relevant JCPD references.

XPS was used to investigate the chemical states and surface compositions of the hollow nickel ferrite nanofibers. The obtained XPS results indicated the presence of Ni, Fe, C, and O in hollow nickel ferrite nanofibers **Figure 5(a-e)**, while C, Ni, Fe, and O were found in the pristine nickel ferrite and C, O and N were found in the multichannel carbon nanofibers (see **Figures S5- S6**). In Figure 5, the deconvoluted C 1s core-level spectra exhibited three peaks at 284.7, 286.6, and 288.6 eV, attributable to C-C, C-O, and C=O, respectively.<sup>53</sup> The Fe 2p spectrum showed two major peaks at 711.71 and 724.41 eV, suggesting the presence of Fe 2p<sub>3/2</sub> and Fe 2p<sub>1/2</sub>, and satellite peaks at 715.88 eV. Similarly, the Ni spectrum is also in agreement with the literature.<sup>54</sup> It shows the split peak characteristic of Ni 2p<sub>1/2</sub> at 854.76 eV and 855.94 eV, with the corresponding satellite peak visible at 860.38 eV. The peak for Ni 2p<sub>3/2</sub> appears at 872.98 eV, with a satellite peak at 879.93 eV. The high-resolution Ni 2p XPS spectrum revealed that Ni is present mainly in the +2 and +3 oxidation states.<sup>55</sup> The XPS of the multichannel carbon nanofibers, the base material, shows a significant amount of nitrogen doping. The deconvoluted N 1s spectrum contains a pyridinic peak at 389.2 eV and pyrrolic peaks at 400.1 eV. The percentage of pyridinic N (peak area 52.27%) was higher than that of pyrrolic N (peak area 47.73%), perhaps because the sample was pyrolyzed at a high temperature of 800 °C.



Quantitative XPS analysis (**Table S2**) reveals that the  $\text{Ni}^{3+}/\text{Ni}^{2+}$  ratio is 2.76 for the hollow  $\text{NiFe}_2\text{O}_4$  nanofiber and 2.79 for the pristine  $\text{NiFe}_2\text{O}_4$  sample, while the  $\text{Fe}^{3+}/\text{Fe}^{2+}$  ratio is 1.64 and 1.69, respectively. These values indicate that the surface oxidation state distribution remains largely unchanged between the two samples. The negligible variation in these ratios suggests that the formation of the hollow morphology does not significantly alter the intrinsic surface chemistry. Therefore, the enhanced catalytic performance is predominantly attributed to morphology-induced effects rather than changes in oxidation state.

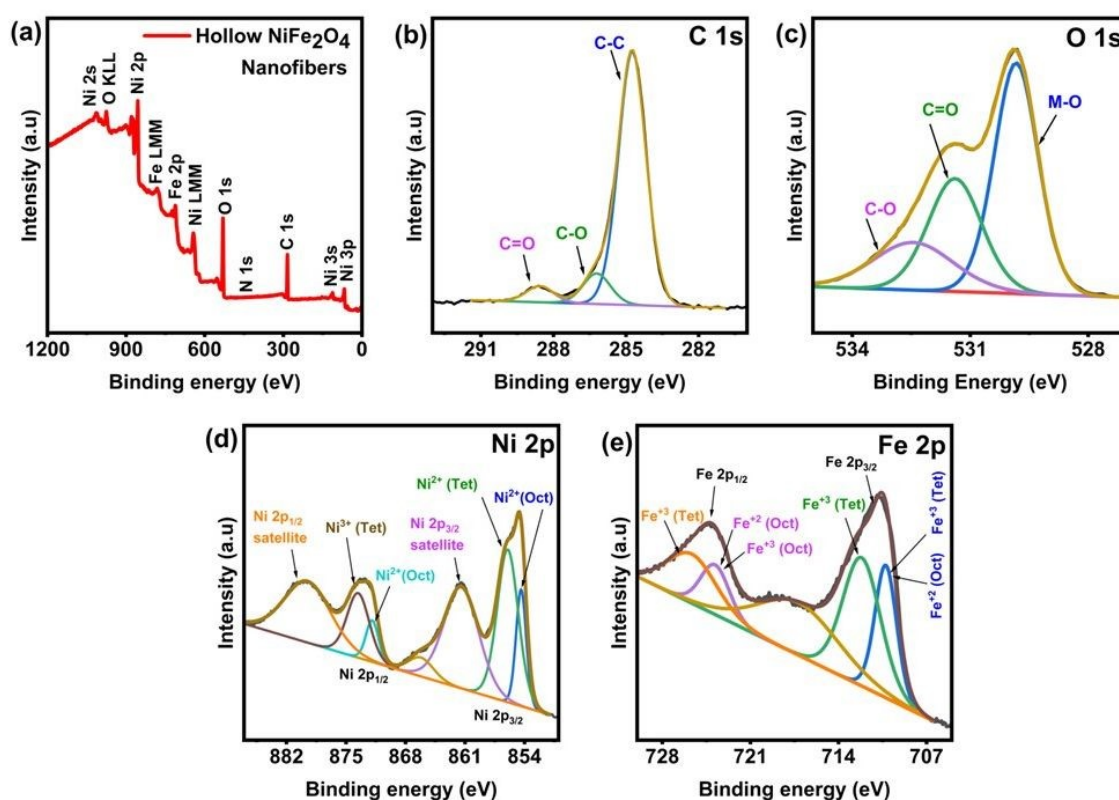


**Figure 5:** Full scan (a) and high-resolution XPS spectra of the hollow  $\text{NiFe}_2\text{O}_4$  nanofibers; (b) C 1s; (c) O 1s; (d) Ni 2p; and (e) Fe 2p.

The Brunauer-Emmett-Teller isotherm shown in **Figure 6** shows that the materials belong to type IV according to IUPAC classification scheme.<sup>56</sup> The formation of a hysteresis loop shows that the materials have mesopores, which undergo multilayer adsorption followed by capillary condensation. The shape of the hysteresis loop defines the shape of the pores. This loop falls under category H3,<sup>57</sup> which suggests that the samples have slit-like pores. The average pore and pore size distribution has been calculated using the Barrett-Joyner-Halenda model, which gave values of 3.95 nm and 5.35 nm in the case of hollow porous nickel ferrite nanofibers and pristine nickel ferrite, respectively. The surface areas of each sample have been calculated from



the isotherm data using the BET equation. The hollow nickel ferrite nanofibers showed a higher surface area of around  $167.037 \text{ m}^2/\text{g}$ , which is double that of the pristine nickel ferrite at  $81.575 \text{ m}^2/\text{g}$ .

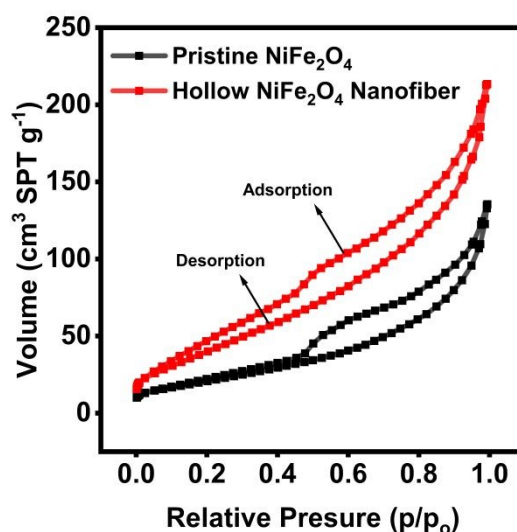


**Figure 6:** Adsorption-desorption isotherms of hollow  $\text{NiFe}_2\text{O}_4$  nanofibers and pristine  $\text{NiFe}_2\text{O}_4$ .

## 2.2 Electrocatalysis for the hydrogen evolution reaction

Owing to the large surface area, porosity, and distinctive morphology of the fabricated hollow porous nickel ferrite nanofibers, they were investigated as an electrocatalyst for the hydrogen evolution reaction using a three-electrode system in highly alkaline media ( $\text{pH} = 13.85$ ). For comparison, the pristine nickel ferrite ( $\text{NiFe}_2\text{O}_4$ ), and multichannel carbon nanofibers were also tested under the same conditions. Cyclic voltammetry was performed over multiple cycles at a scan rate of  $50 \text{ mV s}^{-1}$  until the resulting voltammograms were essentially identical. The linear sweep voltammetry (LSV) curves of the materials at a scan rate of  $5 \text{ mV s}^{-1}$  in  $1 \text{ M KOH}$  without any IR compensation are shown in **Figure 7(a)**. The hollow porous nickel ferrite nanofibers exhibited the lowest overpotential of the tested materials of  $178 \pm 3 \text{ mV}$  at a current density of  $50 \text{ mA cm}^{-2}$ . In the case of pristine nickel ferrite, an overpotential of  $342 \pm 2 \text{ mV}$  was required to reach the same current density, whilst multichannel carbon nanofibers (which were used as the template) required an overpotential of  $294 \pm 5 \text{ mV}$  to reach  $50 \text{ mA cm}^{-2}$ . In the case of just nickel foam, the current density did not reach  $50 \text{ mA cm}^{-2}$  within the test window. The superior performance of the hollow porous nickel ferrite nanofibers is attributed to their high surface area on account of their hollow morphology and highly porous nature.



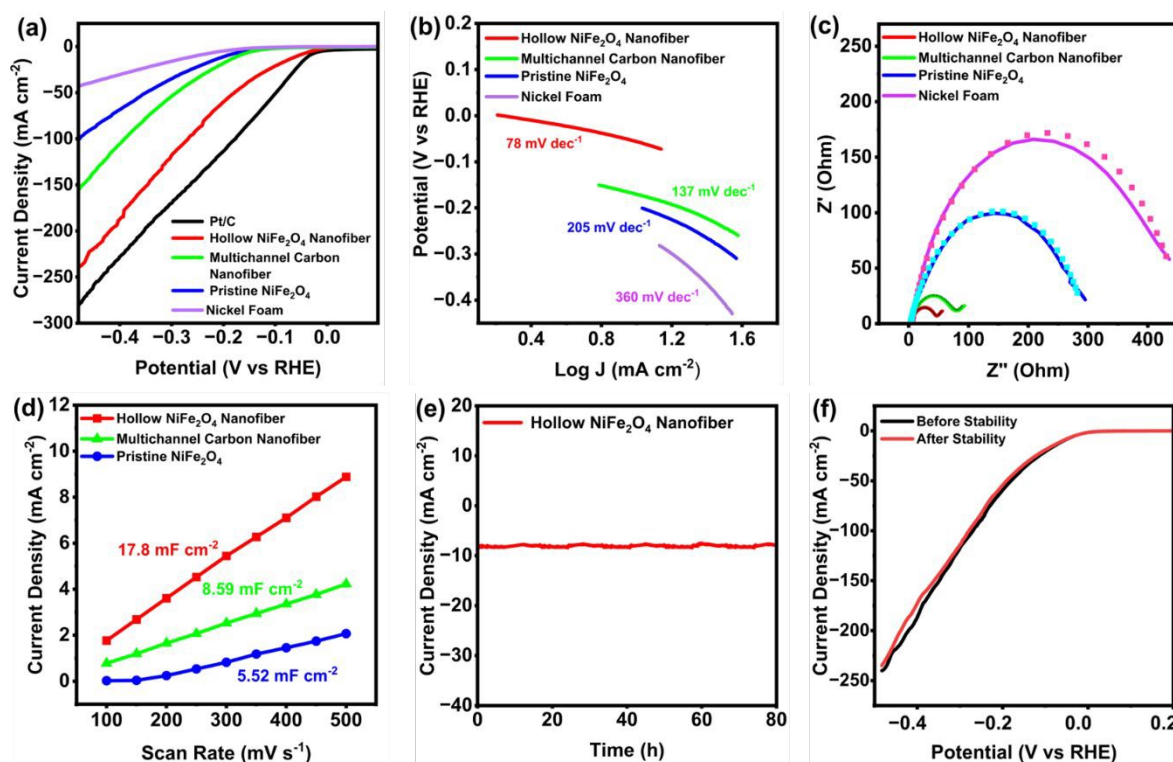


**Fig. 7.** (a) The polarization curves of the as-prepared materials at a scan rate of  $5 \text{ mV s}^{-1}$  in 1 M KOH solution; (b) the corresponding Tafel plots derived from the polarization curves; (c) Nyquist plots (scattered lines; the fitted data from the equivalent circuit model are also shown as solid lines); (d) the linear plots of current density vs. scan rate to calculate the double layer capacitances (Cdl) of the various materials; (e) bulk electrolysis of the hollow  $\text{NiFe}_2\text{O}_4$  nanofibers at  $-0.083 \text{ V}$  vs. RHE for 80 h; and (f) corresponding polarization curves before and after bulk electrolysis at  $-0.083 \text{ V}$  vs. RHE for 80 h.

The Tafel slopes of all the materials were calculated from the linear sweep voltammetry data (**Figure 7(b)**). The hollow nickel ferrite nanofibers gave the lowest Tafel slope of  $78 \text{ mV dec}^{-1}$ , compared to pristine nickel ferrite ( $205 \text{ mV dec}^{-1}$ ), the multichannel carbon nanofibers ( $137 \text{ mV dec}^{-1}$ ), and nickel foam ( $360 \text{ mV dec}^{-1}$ ). The Tafel value of the hollow nickel ferrite nanofibers points towards the Volmer-Heyrovsky mechanism<sup>58</sup> for hydrogen production in which  $\text{H}_{\text{ads}}$  species are first adsorbed on the catalyst surface, and are then subsequently reduced and protonated to release  $\text{H}_2$  molecules. The  $\text{Ni}^{2+}$  ions are considered key sites for  $\text{H}$  and  $\text{OH}^-$  acceptors to accelerate the Volmer reaction, facilitating water dissociation while  $\text{Fe}^{3+}$  ions may assist in stabilizing  $^*\text{H}$  intermediates through water adsorption or enhancing charge transfer during the subsequent step.<sup>59</sup> This synergistic interaction between Ni and Fe is believed to



promote more efficient HER kinetics.<sup>60</sup> Moreover, the hollow porous morphology of the catalyst should make its active sites more accessible and enhance electrolytic diffusion, increasing the overall efficiency of catalyst.<sup>61</sup>

**Figure 7(c)** shows the EIS spectra of the materials over the frequency range from  $10^5$  to 0.1 Hz with an applied potential of  $-0.083$  V vs RHE. The equivalent circuits used to fit the data are shown in **Figure S7**, and **Table S3** shows the value of each component. The hollow nickel ferrite nanofibers exhibited the smallest charge transfer resistance ( $R_{ct}$ ) value of  $42.42 \Omega$  indicating enhanced electrochemical activity. The Nyquist plot reveals significant diffusive behaviour in the hollow nickel ferrite nanofibers and multichannel nanofibers. The equivalent circuits for these nanofiber materials include a constant phase element (CPE) with a Warburg impedance component. In contrast, pristine nickel ferrite exhibits negligible diffusive behaviour and follows a simple constant phase element model suggestive of a less porous structure and more limited pathways for mass transport compared to the two nanofibers. The exchange current density ( $j_0$ ) which reflects the intrinsic charge-transfer kinetics at the electrode–electrolyte interface under equilibrium conditions, was estimated from the charge-transfer resistance ( $R_{ct}$ ) obtained via EIS fitting, using the low-overpotential Butler–Volmer relationship<sup>62</sup> (**Equation: S5**, supplementary information). The hollow nickel ferrite nanofiber catalyst revealed a higher  $j_0$  ( $301 \mu\text{A cm}^{-2}$ ) than that of pristine nickel ferrite ( $43 \mu\text{A cm}^{-2}$ ) indicating enhanced interfacial electron transfer kinetics.

Cyclic voltammetry measurements of the materials were performed at different scan rates within the non-faradaic potential range of  $-0.3$  to  $-0.5$  V versus Hg/HgO in 1 M KOH solution (**Figure S8** in the Supporting Information) to gauge the electrochemical surface area relative to the nickel foam substrate. **Figure 7(d)** shows the double layer capacitance ( $C_{dl}$ ) values of the various materials (see also **Figures S9-S10**). From these values, the corresponding electrochemical surface areas relative to the nickel foam substrate could be calculated as follows: hollow porous  $\text{NiFe}_2\text{O}_4$  nanofibers ( $450 \text{ cm}^2 \text{ per cm}^2_{(\text{geometric})}$ ), pristine nickel ferrite ( $147 \text{ cm}^2 \text{ per cm}^2_{(\text{geometric})}$ ), and multichannel carbon nanofibers ( $222 \text{ cm}^2 \text{ per cm}^2_{(\text{geometric})}$ ). To rule out the contribution of any residual carbon support to the electrochemical surface area of the material, C, H, N elemental analysis of hollow porous  $\text{NiFe}_2\text{O}_4$  was also performed, which showed a carbon content of only 5.80% in the final product after calcination, suggesting that contributions from residual carbon to the effective electrochemical surface area are small. The LSV curves were normalized by the electrochemically active surface area (ECSA) to evaluate the intrinsic catalytic activity of the catalysts (**Figure S11**). Even after normalization with



respect to the ECSA, the hollow porous NiFe<sub>2</sub>O<sub>4</sub> nanofibers maintained superior catalytic performance, suggesting that the enhanced activity is not solely due to increased surface area but also arises from improved intrinsic kinetics. Polarization curves normalized by BET area (**Figure S12**) also confirm the above conclusion that the hollow porous NiFe<sub>2</sub>O<sub>4</sub> nanofibers possesses enhanced intrinsic activity compared to the pristine nickel ferrite.

The stability of the hollow NiFe<sub>2</sub>O<sub>4</sub> nanofiber catalyst was studied using chronopotentiometry at an applied potential of -0.083 V vs RHE for 80 hours. **Figure 7(e)** shows a small decrease in the current density delivered by the catalyst after 80 h in an alkaline medium, showing a good chemical and mechanical stability of the material. The LSV of the electrode taken before and after the stability experiments (**Figure 7(f)**) shows a negligible shift of ~9 mV in the polarization curve, suggesting a measure of functional stability for the hollow nickel ferrite nanofibers for the hydrogen evolution reaction.<sup>63</sup> To evaluate the practical applicability of the catalyst, the stability was further assessed at a high current density of 100 mA cm<sup>-2</sup> for another 60 h by chronopotentiometry as shown in **Figure S13**. Post-stability SEM analysis **Figure S14(a-c)** revealed that the hollow fibrous morphology of NiFe<sub>2</sub>O<sub>4</sub> remains intact after electrolysis. However, slight surface layering was observed, which may be attributed to the presence of the Nafion binder and/or adsorption of KOH electrolyte during extended electrochemical testing. This is further supported by the detection of potassium in the post-stability test energy-dispersive X-ray spectroscopy (EDX) analysis **Figure S14(d)**, while all other constituent elements of the catalyst were also retained. XRD patterns of the electrode were recorded before and after the stability test **Figure S14(e)**. However, the strong diffraction peaks from the nickel foam substrate dominate the spectrum and partially obscure the characteristic peaks of NiFe<sub>2</sub>O<sub>4</sub>, limiting detailed phase analysis.

The catalytic activity was further evaluated by estimating the turnover frequency (TOF) using **Eq. S6** (Supporting Information). The surface concentration of active sites was approximated from the integrated area of the redox peak corresponding to the M<sup>3+</sup>/M<sup>2+</sup> transition (**Figure S15**) as the TOF value depends on the estimation of the number of active sites and is therefore used as an approximate measure of intrinsic activity. The TOF at an overpotential of 200 mV was calculated to be 0.51 s<sup>-1</sup>, which is higher than those reported for previously studied Ni or Fe-based electrocatalysts<sup>64-67</sup> for HER, indicating good intrinsic catalytic activity of the hollow porous NiFe<sub>2</sub>O<sub>4</sub> nanofibers. The Faradaic efficiency of the hollow NiFe<sub>2</sub>O<sub>4</sub> nanofiber catalyst for the hydrogen evolution reaction was also determined by running a controlled potential



electrolysis at  $-0.083$  V vs RHE for 1 h in an H-cell (**Figure S16**) and was found to be  $98 \pm 0.2\%$ .

### 3. Conclusion

A sustainable synthetic approach based on the utilization of waste expanded polystyrene was employed for the synthesis of hollow porous NiFe<sub>2</sub>O<sub>4</sub> nanofibers. These fibers were shown to be effective as an electrocatalyst for the hydrogen evolution reaction. Various characterization techniques were employed, revealing that the catalyst has a uniform morphology throughout the structure and has a higher surface area ( $167$  m<sup>2</sup>/g) compared to the pristine NiFe<sub>2</sub>O<sub>4</sub> ( $81$  m<sup>2</sup>/g). The porous hollow NiFe<sub>2</sub>O<sub>4</sub> nanofibers showed significantly enhanced hydrogen evolution activity at a much lower overpotential of  $178$  mV  $\pm$   $3$  mV (at a current density of  $50$  mA cm<sup>-2</sup> in linear sweep voltammetry), compared to the pristine NiFe<sub>2</sub>O<sub>4</sub> material, which required of  $342$  mV  $\pm$   $2$  mV reach the same current density. The porous hollow NiFe<sub>2</sub>O<sub>4</sub> nanofibers gave a Faradaic efficiency of  $98 \pm 0.2\%$  for hydrogen evolution. These results suggest that waste Styrofoam can be utilized to template the formation of a porous hollow morphology catalyst with promising electrochemical activity.

#### Data availability

The data underpinning this study have been deposited in the University of Glasgow's Enlighten database under accession code <http://dx.doi.org/10.5525/gla.researchdata.XXXX>.

#### CRedit authorship contribution statement

**Rabiya Javed Awan:** Conceptualization, Data curation, Investigation, Methodology, Writing – original draft.

**Zeliha Ertekin:** Investigation, Writing – review & editing.

**Senem Çitoğlu:** Investigation

**Hatice Duran:** Investigation, Writing – review & editing.

**Mark D. Symes:** Conceptualization, Supervision, Writing – review & editing.

**Salman Noshear Arshad:** Conceptualization, Supervision, Writing – review & editing.



## Declaration of Competing Interest

View Article Online  
DOI: 10.1039/D6MA00599C

The authors declare that they have no known competing financial interests or personal relationships that could have appeared to influence the work reported in this paper.

## Supplementary Information

The supplementary information includes data on experimental section, Fourier transform infrared spectrometry (FTIR), nuclear magnetic resonance (NMR), scanning electron microscopy with energy-dispersive X-ray spectroscopy (SEM-EDX) together with elemental mapping, cyclic voltammetry, electrochemical impedance spectroscopy (EIS), and gas chromatography.

## Acknowledgements

We would like to thank Prof. Peter Skabara (University of Glasgow) for use of the electrospinning machine. We thank Dr Christopher Kelly (University of Glasgow) for helpful discussions on BET and XPS analysis. We thank the Geoanalytical Electron Microscopy and Spectroscopy (GEMS) facility in the School of Geographical and Earth Sciences, University of Glasgow for cross-sectional scanning electron microscopy. This work was supported by the EPSRC (EP/W033135/1). RJA would like to thank the Commonwealth Scholarship Commission for a split-site research scholarship. MDS thanks the Royal Society for a University Research Fellowship (URF\R\211007). SNA thanks the early career research grant from KFUPM (ECR251-MSE-354, No. EC2617).

## References

1. Maeda, K.; Teramura, K.; Lu, D.; Takata, T.; Saito, N.; Inoue, Y.; Domen, K., Photocatalyst Releasing Hydrogen from Water. *Nature* **2006**, *440*, 295-295.
2. Zhang, L.; Jia, C.; Bai, F.; Wang, W.; An, S.; Zhao, K.; Li, Z.; Li, J.; Sun, H., A Comprehensive Review of the Promising Clean Energy Carrier: Hydrogen Production, Transportation, Storage, and Utilization (Hptsu) Technologies. *Fuel* **2024**, *355*, 129455.



3. Li, X.; Hao, X.; Abudula, A.; Guan, G., Nanostructured Catalysts for Electrochemical Water Splitting: Current State and Prospects. *Journal of Materials Chemistry A* **2016**, *4*, 11973-12000. View Article Online  
DOI: 10.1039/D6MA00599C
4. Sun, H.; Xu, X.; Kim, H.; Jung, W.; Zhou, W.; Shao, Z., Electrochemical Water Splitting: Bridging the Gaps between Fundamental Research and Industrial Applications. *Energy & Environmental Materials* **2023**, *6*, e12441.
5. Zou, X.; Zhang, Y., Noble Metal-Free Hydrogen Evolution Catalysts for Water Splitting. *Chemical Society Reviews* **2015**, *44*, 5148-5180.
6. Jin, C.; Fu, R.; Ran, L.; Wang, W.; Wang, F.; Zheng, D.; Feng, Q.; Wang, G., Facile Fabrication of Hierarchical Ultrathin Rh-Based Nanosheets for Efficient Hydrogen Evolution. *RSC advances* **2023**, *13*, 13985-13990.
7. Cheng, Z.; Xu, Y.; Fei, B., Noble Metal-Free Ternary Cobalt–Nickel Phosphides for Enhanced Photocatalytic Dye-Sensitized Hydrogen Evolution and Catalytic Mechanism Investigation. *RSC advances* **2023**, *13*, 23638-23647.
8. Yan, Y.; Wang, P.; Lin, J.; Cao, J.; Qi, J., Modification Strategies on Transition Metal-Based Electrocatalysts for Efficient Water Splitting. *Journal of Energy Chemistry* **2021**, *58*, 446-462.
9. Sanati, S.; Morsali, A.; Garcia, H., First-Row Transition Metal-Based Materials Derived from Bimetallic Metal–Organic Frameworks as Highly Efficient Electrocatalysts for Electrochemical Water Splitting. *Energy & Environmental Science* **2022**, *15*, 3119-3151.
10. Kubisztal, J.; Kubisztal, M., Pressed Ni/Mfe2o4 (M= Ni, Co) Powder Compacts for Application as Bifunctional, High-Performance Electrodes in Electrochemical Water Splitting. *International Journal of Hydrogen Energy* **2024**, *56*, 912-923.
11. A. Anantha Krishnan, S. H., M. A. Aneesh Kumar, Revathy B. Nair, Sajith Kurian, M. Ameen Sha and P. S. Arun, Nife2o4: Harnessing Catalytic Potential in Water Splitting. *Catalysis Science & Technology* **2024**, *14*, 6155.
12. Li, Q., Zhu, Y., Cheng, M., Du, L., Zhao, M., Zhang, G., Wang, G., Wang, W., Liu, H., Chen, Y. and Xiao, W., Modular Preparation of Functional Bimetallic Spinel from Metal–Organic Frameworks: A Deep Exploration from Macro and Micro Perspectives. *Journal of Materials Chemistry A* **2024**, *12*, 59.
13. Yu, H.; Sweers, M. E.; Osmieri, L.; Park, J. H.; Kropf, A. J.; Yang, D.; Ma, L.; Lyu, X.; Serov, A.; Cullen, D. A., Synergy between Ni and Fe in Nife Aerogel Oxygen Evolution Reaction Catalyst: In Situ 57 Fe Mössbauer and X-Ray Absorption Spectroscopy Studies. *EES Catalysis* **2025**, *3*, 1229-1245.
14. van der Hoeven, J. E.; Krämer, S.; Dussi, S.; Shirman, T.; Park, K. C. K.; Rycroft, C. H.; Bell, D. C.; Friend, C. M.; Aizenberg, J., On the Origin of Sinter-Resistance and Catalyst Accessibility in Raspberry-Colloid-Templated Catalyst Design. *Advanced Functional Materials* **2021**, *31*, 2106876.
15. Cahyanto, H., Chen, X., Lam, F.L., Iadrat, P., Wattanakit, C., Kidkhunthod, P., Singh, V., Brooker, S., Pang, S., Choi, J. and Yip, A.C., Effective Prevention Ofpalladium Metal Particles Sintering by Histidine Stabilization on Silica Catalyst Support. *Advanced Functional Materials* **2024**, *34*, 2402983.
16. Azadmanjiri, J.; Srivastava, V. K.; Kumar, P.; Wang, J.; Yu, A., Graphene-Supported 2d Transition Metal Oxide Heterostructures. *Journal of Materials Chemistry A* **2018**, *6*, 13509-13537.
17. Kumar, R. S.; Ramakrishnan, S.; Prabhakaran, S.; Kim, A. R.; Kumar, D. R.; Kim, D. H.; Yoo, D. J., Structural, Electronic, and Electrocatalytic Evaluation of Spinel Transition Metal Sulfide Supported Reduced Graphene Oxide. *Journal of Materials Chemistry A* **2022**, *10*, 1999-2011.
18. Ding, Q., Liu, M., Miao, Y.E., Huang, Y. and Liu, T., Electrospun Nickel-Decorated Carbon Nanofiber Membranes as Efficient Electrocatalysts for Hydrogen Evolution Reaction. *Electrochimica Acta* **2015**, *159*, 1-7.
19. Qiu, Y., Zhang, Y., Yu, M., Li, X., Wang, Y., Ma, Z. and Liu, S., Ni–Co–O–S Derived Catalysts on Hierarchical N-Doped Carbon Supports with Strong Interfacial Interactions for Improved Hybrid Water Splitting Performance. *Small* **2024**, *20*, 2310087.



20. Inagaki, M.; Yang, Y.; Kang, F., Carbon Nanofibers Prepared Via Electrospinning. *Advanced materials* **2012**, *24*, 2547-2566. View Article Online  
DOI: 10.1039/D2MA00599C
21. Zhang, B.; Kang, F.; Tarascon, J.-M.; Kim, J.-K., Recent Advances in Electrospun Carbon Nanofibers and Their Application in Electrochemical Energy Storage. *Progress in Materials Science* **2016**, *76*, 319-380.
22. Arshad, S. N.; Naraghi, M.; Chasiotis, I., Strong Carbon Nanofibers from Electrospun Polyacrylonitrile. *Carbon* **2011**, *49*, 1710-1719.
23. He, F.; Wang, Y.; Liu, J.; Yao, X. In *One-Dimensional Carbon Based Nanoreactor Fabrication by Electrospinning for Sustainable Catalysis*, Exploration, Wiley Online Library: 2023; p 20220164.
24. Zhao, Y.; Cao, X.; Jiang, L., Bio-Mimic Multichannel Microtubes by a Facile Method. *Journal of the American Chemical Society* **2007**, *129*, 764-765.
25. Li, L.; Peng, S.; Lee, J. K. Y.; Ji, D.; Srinivasan, M.; Ramakrishna, S., Electrospun Hollow Nanofibers for Advanced Secondary Batteries. *Nano Energy* **2017**, *39*, 111-139.
26. Zhang, C.; Wang, Q.; Li, Z.; Liu, H.; Zhong, L.; Liu, J.; Wang, Z.; Wu, R.; Song, P.; Chen, W. J., Enabling Unconventional "Alternating-Distal" N<sub>2</sub> Reduction Pathway for Efficient Ammonia Electrosynthesis. *Angewandte Chemie International Edition* **2025**, e202502957.
27. Gao, Y.; Xiao, Z.; Kong, D.; Iqbal, R.; Yang, Q.-H.; Zhi, L., N, P Co-Doped Hollow Carbon Nanofiber Membranes with Superior Mass Transfer Property for Trifunctional Metal-Free Electrocatalysis. *Nano Energy* **2019**, *64*, 103879.
28. Sharma, P. J.; Bhakhar, S. A.; Patel, M. N.; Nandpal, M. N.; Bhakhar, K. A.; Patel, S. G.; Sahatiya, P.; Nagaraju, G.; Sumesh, C.; Pataniya, P. M., Binder-Free Nickel-Iron Selenide Catalyst Arrays for Coupling Hydrogen Production with Polyethylene Terephthalate Plastic Electro-Upcycling. *Journal of Materials Chemistry A* **2026**, *14*, 1923-1935.
29. Sharma, P. J.; Bhakhar, S. A.; Nandpal, M. N.; Bhakhar, K. A.; Patel, S. G.; Sahatiya, P.; Sumesh, C.; Pataniya, P. M., Electro-Upcycling of Pet Plastic Coupled with Hydrogen Production Using the Nice@ Nite Electrocatalyst. *Journal of Materials Chemistry A* **2026**, *14*, 3591-3604.
30. Chen, X.; Tang, X.; Zhu, G.; Ye, D.; Wan, Q.; Jiang, W.; Zhuang, X.; Ke, C., A Nifeco-Based Self-Supported Anode Fabricated by Hydrogen-Thermal Reduction for Anion Exchange Membrane Water Electrolysis. *ACS Applied Energy Materials* **2026**.
31. Huang, C.; Thomas, N. L., Fabrication of Porous Fibers Via Electrospinning: Strategies and Applications. *Polymer Reviews* **2020**, *60*, 595-647.
32. Chandra, M.; Kohn, C.; Pawlitz, J.; Powell, G., Real Cost of Styrofoam. *Saint Louis University MGT* **2016**, 6006-02.
33. Maafa, I. M., Pyrolysis of Polystyrene Waste: A Review. *Polymers* **2021**, *13*, 225.
34. Ho, B. T.; Roberts, T. K.; Lucas, S., An Overview on Biodegradation of Polystyrene and Modified Polystyrene: The Microbial Approach. *Critical reviews in biotechnology* **2018**, *38*, 308-320.
35. Li, T.; Luo, G.; Liu, K.; Li, X.; Sun, D.; Xu, L.; Li, Y.; Tang, Y., Encapsulation of Ni<sub>3</sub>fe Nanoparticles in N-Doped Carbon Nanotube-Grafted Carbon Nanofibers as High-Efficiency Hydrogen Evolution Electrocatalysts. *Advanced Functional Materials* **2018**, *28*, 1805828.
36. Xiao, C.; Zhang, X.; Li, S.; Suryanto, B. H.; MacFarlane, D. R., In Situ Synthesis of Core-Shell-Ni<sub>3</sub>fe (Oh) 9/Ni<sub>3</sub>fe Hybrid Nanostructures as Highly Active and Stable Bifunctional Catalysts for Water Electrolysis. *ACS Applied Energy Materials* **2018**, *1*, 986-992.
37. Zhang, X.; Xu, H.; Li, X.; Li, Y.; Yang, T.; Liang, Y., Facile Synthesis of Nickel-Iron/Nanocarbon Hybrids as Advanced Electrocatalysts for Efficient Water Splitting. *ACS Catalysis* **2016**, *6*, 580-588.
38. Navadeepthy, D.; Rebekah, A.; Viswanthan, C.; Ponpandian, N., Boosting the Kinetics of Oxygen and Hydrogen Evolution in Alkaline Water Splitting Using Nickel Ferrite/N-Graphene Nanocomposite as a Bifunctional Electrocatalyst. *International Journal of Hydrogen Energy* **2021**, *46*, 21512-21524.
39. Shahid, M., Hydrothermally Synthesized Double Layered Ferrite and Its Cnts Anchored Nanoarchitecture: A Novel Water Splitting Electrocatalyst. *Materials Science and Engineering: B* **2024**, *300*, 117143.



40. Zhang, J.; Jiang, Y.; Wang, Y.; Yu, C.; Cui, J.; Wu, J.; Shu, X.; Qin, Y.; Sun, J.; Yan, J., Ultrathin Carbon Coated Mesoporous Ni-NiFe<sub>2</sub>O<sub>4</sub> Nanosheet Arrays for Efficient Overall Water Splitting. *Electrochimica Acta* **2019**, *321*, 134652.
41. Pham, T. N.; Samikannu, A.; Vincze, Z.; Zettinig, P.; Tesfalidet, S.; Wågberg, T.; Mikkola, J. P., Core–Shell Carbon Nanofibers-NiFe Structure on 3d Porous Carbon Foam: Facilitating a Promising Trajectory toward Decarbonizing Energy Production. *Advanced Sustainable Systems* **2022**, *6*, 2200310.
42. Shinde, P. V.; Mane, P.; Chakraborty, B.; Rout, C. S., Spinel NiFe<sub>2</sub>O<sub>4</sub> Nanoparticles Decorated 2d Ti<sub>3</sub>C<sub>2</sub> Mxene Sheets for Efficient Water Splitting: Experiments and Theories. *Journal of Colloid and Interface Science* **2021**, *602*, 232-241.
43. Srinivas, K.; Chen, Y.; Wang, B.; Yu, B.; Lu, Y.; Su, Z.; Zhang, W.; Yang, D., Metal–Organic Framework-Derived Fe-Doped Ni<sub>3</sub>Fe/NiFe<sub>2</sub>O<sub>4</sub> Heteronanoparticle-Decorated Carbon Nanotube Network as a Highly Efficient and Durable Bifunctional Electrocatalyst. *ACS Applied Materials & Interfaces* **2020**, *12*, 55782-55794.
44. Kumar, A.; Bhattacharyya, S., Porous NiFe-Oxide Nanocubes as Bifunctional Electrocatalysts for Efficient Water-Splitting. *ACS applied materials & interfaces* **2017**, *9*, 41906-41915.
45. Hansen, C. M., *Hansen Solubility Parameters: A User's Handbook*; CRC press, 2007.
46. Skvortsov, I. Y.; Malkin, A. Y.; Kuzin, M.; Bondarenko, G.; Gerasimenko, P.; Litmanovich, E., Rheology and Molecular Interactions in Polyacrylonitrile Solutions: Role of a Solvent. *Journal of Molecular Liquids* **2022**, *364*, 119938.
47. Álvarez-Gómez, A.; Yuan, J.; Fernández-Blázquez, J. P.; San-Miguel, V.; Serrano, M. B., Polyacrylonitrile-B-Polystyrene Block Copolymer-Derived Hierarchical Porous Carbon Materials for Supercapacitor. *Polymers* **2022**, *14*, 5109.
48. Deeney, C.; Wang, S.; Belhout, S. A.; Gowen, A.; Rodriguez, B. J.; Redmond, G.; Quinn, S. J., Templated Microwave Synthesis of Luminescent Carbon Nanofibers. *RSC advances* **2018**, *8*, 12907-12917.
49. Zhang, C., Fu, L., Liu, N., Liu, M., Wang, Y. and Liu, Z., Synthesis of Nitrogen-Doped Graphene Using Embedded Carbon and Nitrogen Sources. *Advanced Materials* **2011**, *23*, 1020-1024.
50. Cheng, W.; Tang, K.; Qi, Y.; Sheng, J.; Liu, Z., One-Step Synthesis of Superparamagnetic Monodisperse Porous Fe<sub>3</sub>O<sub>4</sub> Hollow and Core-Shell Spheres. *Journal of Materials Chemistry* **2010**, *20*, 1799-1805.
51. Hu, C.; Gao, Z.; Yang, X., One-Pot Low Temperature Synthesis of MFe<sub>2</sub>O<sub>4</sub> (M= Co, Ni, Zn) Superparamagnetic Nanocrystals. *Journal of Magnetism and Magnetic Materials* **2008**, *320*, L70-L73.
52. Nguyen, M. D.; Attanayake, S. B.; Chinwangso, P.; Hoijang, S.; Qin, C.; Bao, J.; Phan, M.-H.; Lee, T. R., Nickel–Zinc Ferrite Nanoparticles for Hyperthermia: Preserving Superparamagnetism across a Broad Range of Particle Sizes. *ACS Applied Materials & Interfaces* **2025**, *17*, 22929-22940.
53. Askari, M. B.; Salarizadeh, P., Binary Nickel Ferrite Oxide (NiFe<sub>2</sub>O<sub>4</sub>) Nanoparticles Coated on Reduced Graphene Oxide as Stable and High-Performance Asymmetric Supercapacitor Electrode Material. *International Journal of Hydrogen Energy* **2020**, *45*, 27482-27491.
54. Naushad, M.; Ahamad, T.; Al-Maswari, B. M.; Alqadami, A. A.; Alshehri, S. M., Nickel Ferrite Bearing Nitrogen-Doped Mesoporous Carbon as Efficient Adsorbent for the Removal of Highly Toxic Metal Ion from Aqueous Medium. *Chemical Engineering Journal* **2017**, *330*, 1351-1360.
55. Zheng, L.; Gao, S.; Yao, S.; Huang, Y.; Zhai, S.; Hao, J.; Fu, X.; An, Q.; Xiao, Z., N-Doped Porous Carbon with Zif-67-Derived CoFe<sub>2</sub>O<sub>4</sub>-Fe Particles for Supercapacitors. *Journal of Colloid and Interface Science* **2024**, *674*, 735-744.
56. Schlumberger, C.; Thommes, M., Characterization of Hierarchically Ordered Porous Materials by Physisorption and Mercury Porosimetry—a Tutorial Review. *Advanced Materials Interfaces* **2021**, *8*, 2002181.



57. Thommes, M.; Kaneko, K.; Neimark, A. V.; Olivier, J. P.; Rodriguez-Reinos, F.; Rouquerol, J.; Sing, K. S., Physisorption of Gases, with Special Reference to the Evaluation of Surface Area and Pore Size Distribution (Iupac Technical Report). *Pure and applied chemistry* **2015**, *87*, 1051-1069. View Article Online  
DOI: 10.1039/D5MA00599C
58. Lasia, A., Mechanism and Kinetics of the Hydrogen Evolution Reaction. *International Journal of Hydrogen Energy* **2019**, *44*, 19484.
59. Fan, C.; Zhai, X.; Chen, L.; Peng, S.; Jiang, R.; Yu, J.; Li, Y.; Zhang, Y.; Kong, W.; Ge, G., Synthesis and Electrocatalytic Mechanism of Ultrafine MFe<sub>2</sub>O<sub>4</sub> (M: Co, Ni, and Zn) Nanocrystallites: M/Fe Synergistic Effects on the Electrochemical Detection of Cu (II) and Hydrogen Evolution Reaction Performances. *Journal of Materials Chemistry A* **2021**, *9*, 22277-22290.
60. Messaoudi, Y.; Belhadj, H.; Khelladi, M. R.; Azizi, A., Rational Design of NiFe Alloys for Efficient Electrochemical Hydrogen Evolution Reaction: Effects of Ni/Fe Molar Ratios. *RSC advances* **2022**, *12*, 29143-29150.
61. Park, J.; Kwon, T.; Kim, J.; Jin, H.; Kim, H. Y.; Kim, B.; Joo, S. H.; Lee, K., Hollow Nanoparticles as Emerging Electrocatalysts for Renewable Energy Conversion Reactions. *Chemical Society Reviews* **2018**, *47*, 8173-8202.
62. Barsoukov, E., *Impedance Spectroscopy Theory, Experiment, and Applications*; Wiley Online Library, 2005.
63. Chen, Y.; Chen, J.; Bai, K.; Xiao, Z.; Fan, S., A Flow-through Electrode for Hydrogen Production from Water Splitting by Mitigating Bubble Induced Overpotential. *Journal of Power Sources* **2023**, *561*, 232733.
64. Mukherjee, A.; Chakrabarty, S.; Su, W.-N.; Basu, S., Nanostructured Nickel Ferrite Embedded in Reduced Graphene Oxide for Electrocatalytic Hydrogen Evolution Reaction. *Materials today energy* **2018**, *8*, 118-124.
65. Khan, N. A.; Rahman, G.; Chae, S. Y.; Yoon, N.; Shah, A. u. H. A.; Mian, S. A., Unraveling the Electrocatalytic Response of Zn-Substituted Nickel Ferrite for Overall Water Splitting. *ACS Applied Energy Materials* **2024**, *7*, 4960-4974.
66. McKone, J. R.; Sadtler, B. F.; Werlang, C. A.; Lewis, N. S.; Gray, H. B., Ni-Mo Nanopowders for Efficient Electrochemical Hydrogen Evolution. *ACS catalysis* **2013**, *3*, 166-169.
67. Pan, Y.; Hu, W.; Liu, D.; Liu, Y.; Liu, C., Carbon Nanotubes Decorated with Nickel Phosphide Nanoparticles as Efficient Nanohybrid Electrocatalysts for the Hydrogen Evolution Reaction. *Journal of Materials Chemistry A* **2015**, *3*, 13087-13094.



The data underpinning this study will be deposited in the University of Glasgow's Enlighten database, and an accession code will be included in the manuscript after peer review is complete, which will take the readers to the data. A placeholder for this has been added to the manuscript. Data will be available through Enlighten free of charge and free of access barriers for at least 10 years, as mandated by UK public sector funders.

In addition, we supply a file of supplementary information with this submission, which includes data on experimental section, Fourier transform infrared spectrometry (FTIR), nuclear magnetic resonance (NMR), scanning electron microscopy with energy-dispersive X-ray spectroscopy (SEM-EDX) together with elemental mapping, cyclic voltammetry, electrochemical impedance spectroscopy (EIS), and gas chromatography.

